RESEARCH ARTICLE

NANO · MICRO small
www.small-journal.com

H-Glass Supported Hybrid Gold Nano-Islands for Visible-Light-Driven Hydrogen Evolution

Indrajeet Mandal, Jagannath Gangareddy, Abimannan Sethurajaperumal, Murugasenapathi NK, Manikanta Majji, Susmita Bera, Pratyasha Rudra, Vanmathi Ravichandran, Sandip Bysakh, Noah Jacob, K. D. M. Rao, Rajiv K. Singh, N. M. Anoop Krishnan, Manohar Chirumamilla, Tamilarasan Palanisamy,* M. Motapothula,* Eswaraiah Varrla,* Srabanti Ghosh,* and Amarnath R. Allu**

Flat panel reactors, coated with photocatalytic materials, offer a sustainable approach for the commercial production of hydrogen (H_2) with zero carbon footprint. Despite this, achieving high solar-to-hydrogen (STH) conversion efficiency with these reactors is still a significant challenge due to the low utilization efficiency of solar light and rapid charge recombination. Herein, hybrid gold nano-islands (HGNIs) are developed on transparent glass support to improve the STH efficiency. Plasmonic HGNIs are grown on an in-house developed active glass sheet composed of sodium aluminum phosphosilicate oxide glass (H-glass) using the thermal dewetting method at 550 °C under an ambient atmosphere. HGNIs with various oxidation states (Au^0, Au^+, and Au^-) and multiple interfaces are obtained due to the diffusion of the elements from the glass structure, which also facilitates the lifetime of the hot electron to be ≈2.94 ps. H-glass-supported HGNIs demonstrate significant STH conversion efficiency of 0.6%, without any sacrificial agents, via water dissociation. This study unveils the specific role of H-glass-supported HGNIs in facilitating light-driven chemical conversions, offering new avenues for the development of high-performance photocatalysts in various chemical conversion reactions for large-scale commercial applications.

1. Introduction

Hydrogen (H_2) is the key to a sustainable energy future.[1] Its ability to emit only water as a byproduct makes it an attractive alternative to fossil fuels, and its adaptability in many industrial applications adds to its value.[2] However, the current methods of H_2 production are not sustainable since 95% of H_2 is produced through processes emitting large amounts of CO_2, hindering efforts to combat climate change.[3–6] The global production of H_2 currently stands at 100 million tons annually, but this comes at the cost of 930 million tons of CO_2 emission.[7,8] The current H_2 production methods with zero carbon footprint are not scalable at the industrial level.[9,10] A significant focus has been placed on increasing the production of green H_2, using abundant solar energy and readily available water sources.[10] However, a key necessity for H_2 production from water without external assistance is a highly efficient

I. Mandal, J. Gangareddy, P. Rudra, S. Bysakh, S. Ghosh, A. R. Allu
CSIR-Central Glass and Ceramic Research Institute
196 Raja S C Mullick Road, Kolkata 700 032, India
E-mail: srabanti@cgcri.res.in; aareddy@cgcri.res.in

A. Sethurajaperumal, V. Ravichandran, E. Varrla
Sustainable Nanomaterials and Technologies Lab
Department of Physics and Nanotechnology
SRM Institute of Science and Technology
Kattankulathur, Chengalpattu, Tamil Nadu 603203, India
E-mail: eswarail@srmist.edu.in

The ORCID identification number(s) for the author(s) of this article can be found under https://doi.org/10.1002/smll.202401131

DOI: 10.1002/smll.202401131

M. NK, T. Palanisamy
Electrodics and Electrocatalysis Division (EEC)
CSIR-Central Electrochemical Research Institute (CECRI)
Karaikudi, Tamil Nadu 630003, India
E-mail: tamilan@cecri.res.in

M. NK, P. Rudra, R. K. Singh, T. Palanisamy, S. Ghosh, A. R. Allu
Academy of Scientific and Innovative Research (AcSIR)
Ghaziabad 201002, India

M. Majji, N. Jacob, M. Motapothula
Department of Physics
SRM University AP
Amaravati, Andhra Pradesh 522502, India
E-mail: mallikarjuna.m@srmap.edu.in

S. Bera
Research Institute for Sustainable Energy (RISE)
TCG Centres for Research and Education in Science and Technology (TCG CREST)
Sector V, Salt Lake, Kolkata 700091, India

and stable photocatalyst capable of driving the necessary redox reactions.[11–16]

To date, various photocatalytic materials have been proposed, designed, and developed accordingly.[17,18] Where most of these traditional photocatalysts require a sacrificial agent to function, and their effectiveness in H_2 production often depends on cocatalysts that enhance the absorption of solar energy, spanning from ultraviolet (UV) to visible light.[19,20] Further, various challenges like light scattering, limited penetration depth, suboptimal absorption, and rapid charge recombination collectively hinder conversion efficiencies.[21] To overcome these challenges, thin photocatalytic films were developed. These films offer effective light absorption, made possible by designing catalysts to enhance light penetration and maximize surface area while minimizing the amount of photocatalyst used.[22] A notable development in this field is flat panel reactors, where the flat glass panels coated with thin sheets of photocatalytic material demonstrate significant potential.[21,23] Xiong et al.[24] reported on panel-type reactors with dimensions of 5×5 cm^2, using flat frosted glass plates coated with a $Rh_{2-y}Cr_yO_3/(Ga_{1-x}Zn_x)(N_{1-x}O_x)$ photocatalyst, further enhanced with hydrophilic silica particles to improve the solar-to-hydrogen (STH) efficiency. Additionally, Goto et al.[25] designed a 1×1 m^2 flat panel reactor incorporating silica-modified Al-doped $SrTiO_3$ photocatalysts, achieving an STH conversion efficiency of 0.4% under natural sunlight. However, achieving a significantly higher STH conversion efficiency, in the range of 5–10%, remains crucial for the commercial viability of these flat panel reactors.[23]

Numerous studies have highlighted the ability of plasmonic metal nanoparticles (MNPs) to catalyze chemical reactions when exposed to low-intensity visible light.[26–28] Moreover, the choice of supporting materials plays a vital role, significantly influencing the catalytic performance of MNPs.[29,30] For instance, Au NPs demonstrate a higher H_2 dissociation rate when deposited on a dielectric SiO_2 substrate compared to a semiconductor TiO_2 substrate.[31] This difference is attributed to the formation of the Schottky barrier at the metal-semiconductor interface, which in the case of AuNP/TiO_2, facilitates the flow of hot electrons to the TiO_2, thereby limiting the electrons available for catalytic activity. On the other hand, with AuNP/SiO_2, the absence of such a barrier permits more electrons to participate in H_2 dissociation, suggesting that dielectric supports can potentially enhance the photocatalytic efficiency of MNPs. This demonstrates that dielectric glass materials, by facilitating electron availability, may improve the photocatalytic capabilities of MNPs. Therefore, by integrating MNPs onto flat panel glass system, the STH efficiency can be significantly advanced. Further, extensive research highlights the significant role of charge states in determining the catalytic efficiency of Au NPs.[32,33] Among them, multimetallic single nanoparticles (MSNPs) with various interfaces have shown great promise in catalysis applications.[34,35] However, the synthesis of MSNPs has often involved complex and expensive techniques, such as scanning probe block copolymer lithography, solution-phase epitaxial growth, seed-mediated synthesis, and wet-chemical methods.[35–38] This highlights the need for a simple and robust method to synthesize single multielement MNPs that possess multiple charge states and interfaces.

Herein, we introduce hybrid gold nano-islands (HGNIs) as promising photocatalytic material for visible-light-driven water splitting to produce H_2. Metal nano-islands (MNIs) are grown on the glass substrate by cost-effective thermal dewetting process. However, noble metals, known for their chemical inertness, often struggle to bond effectively with most of the glass systems,[39] raising concerns about the stability of MNIs. As a result, there has been limited exploration into the interaction between MNIs and glass, and their potential in photocatalytic activity. Recently, however, a breakthrough was made with the development of a sodium aluminum phosphosilicate glass, referred to as H-glass.[39] This glass system significantly improves the stability of MNIs, through the interaction of glass elements, like phosphorous (P), silicon (Si), Aluminum (Al), and sodium (Na), with MNIs, altering some of the metallic Au into cationic and anionic forms. This creates multiple interfaces between the different forms of Au, resulting in the formation of HGNIs.[34,35] These findings lead us to hypothesize that H-glass-supported HGNIs might be highly effective as photocatalytic active sites for chemical reactions.

This work uncovers the chemical interaction between amorphous glass and Au nanoislands, revealing the existence of nanoislands with multiple Au oxidation states and interfaces. H-glass-supported HGNIs exhibit excellent photocatalytic efficacy for H_2 generation using water/moisture. Consequently, the combination of H-glass with HGNIs is identified as an optimal approach to enhance the photocatalytic performance of the flat glass panel photoreactors tailored for H_2 production. Therefore, by advancing the current state-of-the-art H_2 generation methods, and implementing them on a larger scale, it is possible to achieve next-generation production technologies for clean H_2 with zero-carbon emissions.

2. Results and Discussion

The process of depositing HGNIs on H-glass is outlined in **Figure 1a**. This involves a two-step method: first, applying a 50 nm Au film via sputtering technique, and second, heating it to 550 °C for 15 min under an ambient air environment.

K. D. M. Rao
School of Applied & Interdisciplinary Sciences
Indian Association for the Cultivation of Science
2A & 2B Raja S. C. Mullick Road, Jadavpur, Kolkata 700032, India
R. K. Singh
Photovoltaic Metrology Section
Advanced Material and Devices Metrology Division
CSIR-National Physical Laboratory
New Delhi 110012, India
N. M. A. Krishnan
Department of Civil Engineering
Indian Institute of Technology Delhi
New Delhi 110016, India
M. Chirumamilla
Department of Materials and Production
Aalborg University
Skjernvej 4A, Aalborg 9220, Denmark
E-mail: mch@mp.aau.dk
M. Chirumamilla
Institute of Optical and Electronic Materials
Hamburg University of Technology
Eissendorfer Strasse 38, 21073 Hamburg, Germany

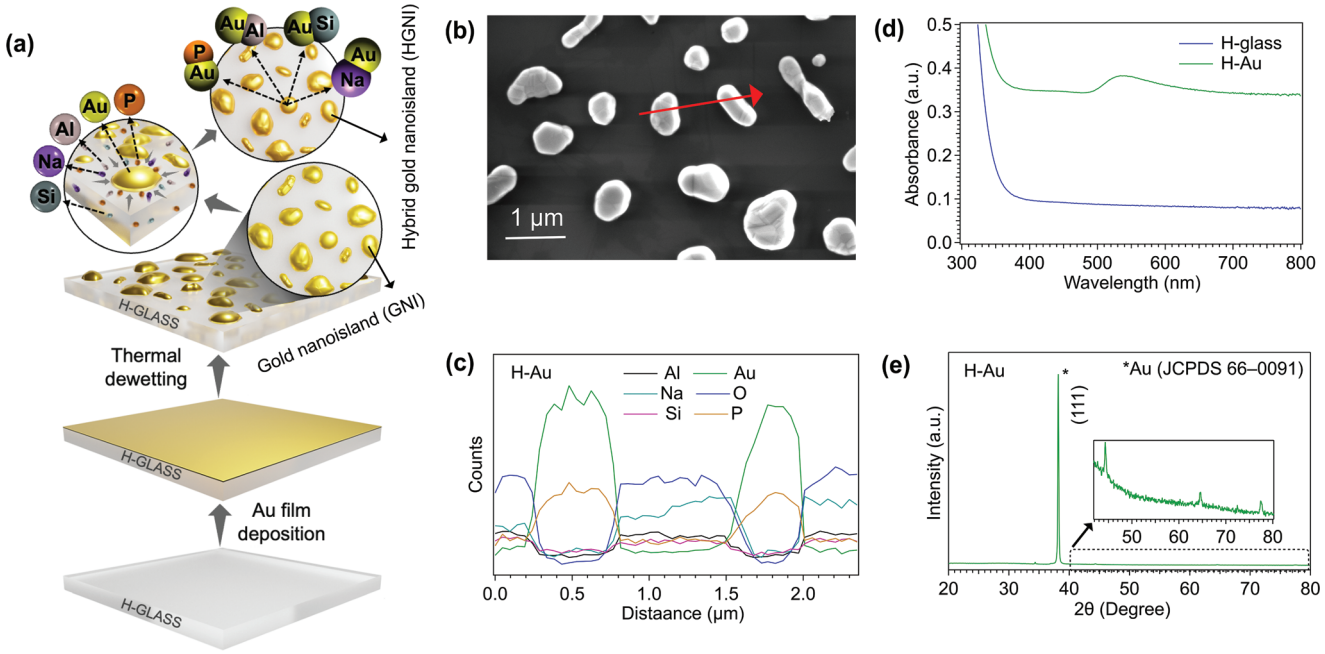

Figure 1. a) The schematic illustration outlining the synthesis procedure used to form HGNIs on an in-house developed H-glass substrate. b) A FESEM image for the H-Au glass. c) EDS line profile taken on the FESEM image (b) for Au, P, Al, Na, Si, and O across the two islands marked with a red arrow. d) UV–vis absorbance spectra of H-glass and H-Au glass. e) XRD pattern for the H-Au glass, inset shows the magnified view.

The structure of the glass network undergoes isotropic expansion once the temperature surpasses the glass transition temperature range. In this context, H-glass coated with Au-film expands isotopically upon being subjected to a heat treatment at a temperature of 550 °C, which is 80 °C above its glass transition temperature (470 °C), Figure S1b (Supporting Information). Consequently, it becomes evident that the GNIs formed during the thermal dewetting process become embedded within the H-glass. This is facilitated by the significantly higher density of Au (19.3 g/cc) compared to that of H-glass (2.5 g/cc). As the substrate cools from 550 °C to room temperature, the glass solidifies, effectively submerging the GNIs within it. As presented in the following sections, these GNIs interact with the glass components and convert them into HGNIs, with multiple elements and Au oxidation states. The resulting H-glass with embedded HGNIs is termed "H-Au". Figure 1b shows a field emission scanning electron microscopy (FE-SEM) image of the HGNIs, as mostly hemispherical isolated islands on the glass surface, though some irregularities are present. Figure 1c, through energy dispersive X-ray spectroscopy (EDS) line-scan data, reveals phosphorus (P) and Au content predominantly in HGNIs. Figure 1d indicates that H-Au glass has a distinct absorption peak due to the localized surface plasmon resonance (LSPR) of the HGNIs. Figure 1e shows X-ray diffraction (XRD) spectra of H-Au glass, confirming a prominent diffraction peak at a 2θ of 38.1° and other peaks at 44.3°, 64.6°, and 77.4°, aligning with the (111), (200), (220), and (311) planes of face-centered cubic (FCC) lattice of Au.[39] HGNIs demonstrate outstanding structural robustness when subjected to a high-power ultrasonication in aqueous media (Figures S2–S8, Supporting Information).

Figures 2a and S9a (Supporting Information) show the cross-sectional transmission electron microscopy (TEM) image of isolated HGNIs. High-resolution-transmission electron microscopy (HR-TEM) images (Figures 2b; Figures S10–S15, Supporting Information) were taken from regions where electron beam transparency was possible, as highlighted in Figure 2a,c shows the fast Fourier transform (FFT) and inverse FFT (IFFT) analyses on specific regions marked in Figure 2b(i),(ii). The resulting lattice spacings were determined to be 0.45 nm and 0.24 nm, respectively. Further analysis of the HR-TEM investigations across various regions (Figure S10, Supporting Information) showed lattice fringes with d-spacings of 0.23 and 0.26 nm. Additionally, the presence of two fringe patterns with d-spacing values of 0.23 and 0.26 nm intersecting at a 75° angle (Figure S11, Supporting Information) emphasizes the complex structural characteristics of HGNIs. By examining multiple HR-TEM images (Figures S12–S17 and Movie S1, Supporting Information), the existence of lattice fringes with different d-spacing values is confirmed. Lattice fringes with 0.24 nm d-spacing are unambiguously attributed to the (111) lattice plane of FCC Au. Owing to the complex chemical composition of HGNIs on H-Au glass, other d-spacing values could not be assigned to specific lattice planes. Nevertheless, the variations in d-spacing are likely linked to the formation of Au compounds,[34,40] $Au_{1-x}M_x$, where M = Al, P, Na, Si.

The chemical composition of the individual HGNIs is evaluated by scanning transmission electron microscopy (STEM), -and the corresponding images are shown in Figure 2d,g for HGNIs that are attached to H-glass and those exposed to air, respectively. The corresponding high-angle annular dark-field (HAADF) images are shown in Figure 2e,h, and the EDS elemental line profiles are shown in Figure 2f,i, respectively. The elemental mappings (Figures S18 and S19, Supporting Information) corresponding to the HGNIs shown in Figure 2d,g distinctly demonstrates the presence of elements P, Au, and Al. These

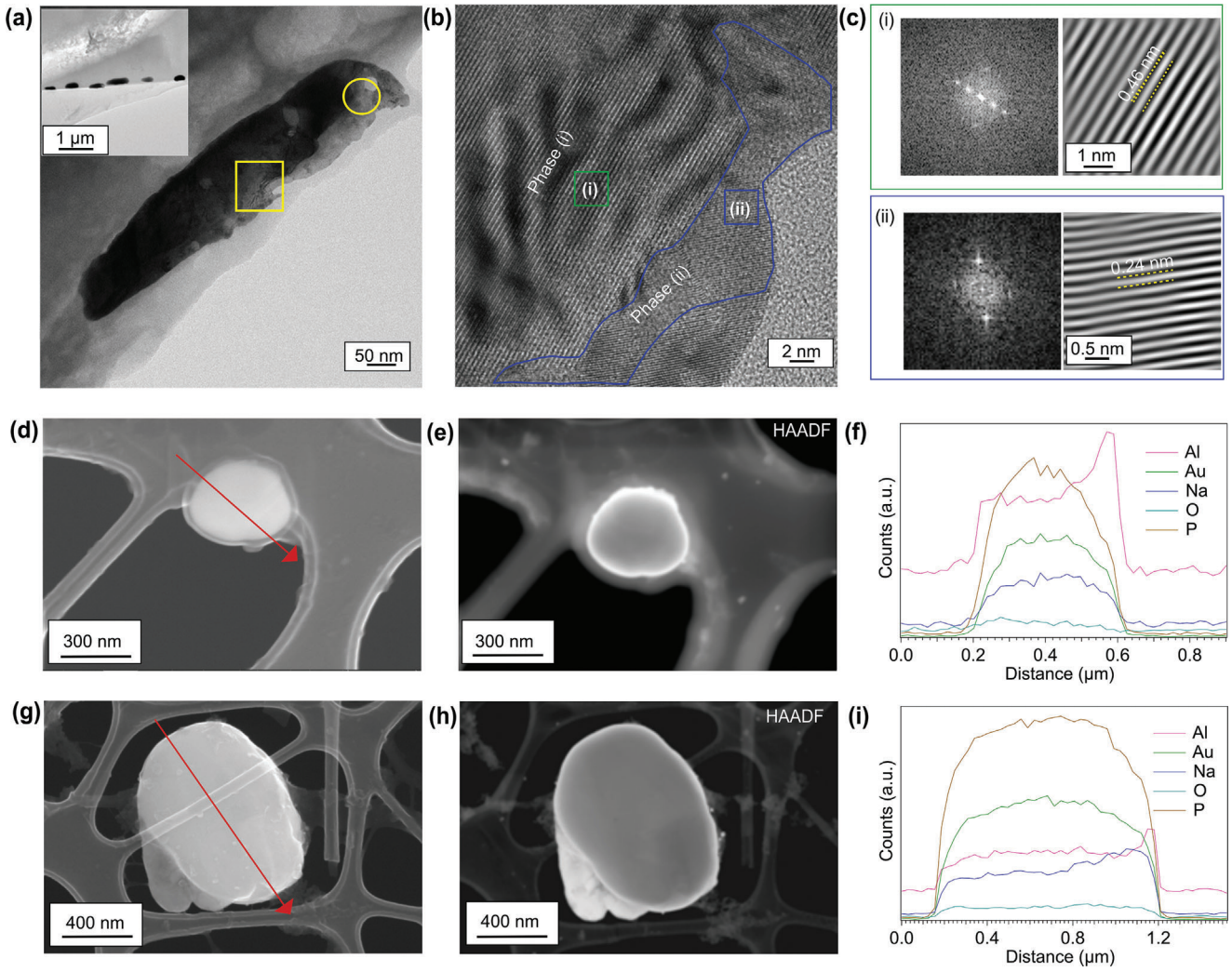

Figure 2. a) A typical cross-sectional TEM image of isolated HGNI, the inset shows a cross-sectional TEM image. Inset shows the low resolution cross-sectional TEM image of H-Au glass. b) HR-TEM image for the region marked with the yellow box in (a). Roman numbers (i) and (ii) in (b) represent different d-space zones in the HGNI. The HR-TEM image for the region marked with the yellow circle in (b) is also shown in Figure S17 (Supporting Information). c) FFT transformations for the regions (i) and (ii) are highlighted in (b). d and g) STEM images for two different isolated HGNIs extracted from H-Au. e and h) High-angle annular dark-field (HAADF) images for the image shown in (d) and (g), respectively. f and i) EDS line profile for Al, Na, Au, P, and O across the islands marked with an arrow in (d) and (g), respectively.

observations suggest that the GNIs within H-glass undergo chemical reactions with components of H-glass under the annealing phase, leading to the diffusion of elements from H-glass into the GNIs and their eventual transformation into HGNIs. The elemental line profile (Figure 2f,i), along with mapping analysis (Figure S18, Supporting Information) and chemical analysis (Figure S19, Supporting Information) at varying electron accelerating voltages, confirms the presence of Si, Al, Na, and P in HGNIs. Further, the presence of these elements in the HGNIs is confirmed by WDS and XPS depth profile analysis.

Figures 3a and S20 (Supporting Information) provide a qualitative chemical analysis of H-glass-supported HGNIs using the wavelength dispersive spectroscopy (WDS) technique. This analysis reveals the presence of elements such as Al, Si, P, Au, and Na in each HGNI. Importantly, the ratio of these elements varies when the electron accelerating voltage is increased from 10 to 20 kV, suggesting a gradient in their concentration levels. Further, X-ray photoelectron spectroscopy (XPS) depth profiling using Ar^+ sputtering was performed on H-Au to investigate the electronic states of elements. Figure 3b–d display the XPS spectra of Au 4f, Na 1s, and P 2p at different depths (see Figures S21 and S22, Supporting Information for the XPS spectra of O 1s, Si 2p, and Al 2p). Irrespective of the depth, Au 4f XPS spectra (Figure 3b) display a clearly separated doublet (by 3.7 eV) corresponding to the spin-orbit coupling of $4f_{7/2}$ and $4f_{5/2}$ states. With increased Ar^+ sputtering time, depth profiling indicates a shift of the Au 4f peak toward higher binding energies, alongside an increase in peak width and intensity. Further, the deconvolution of the Au 4f spectra (Figure 3e; Figure S23, Supporting Information) identifies three distinct Au species with binding energies ≈82.38, 83.18, and 83.98 eV. Following the charge potential model,[41] which posits that metal binding energies rise with a reduction in

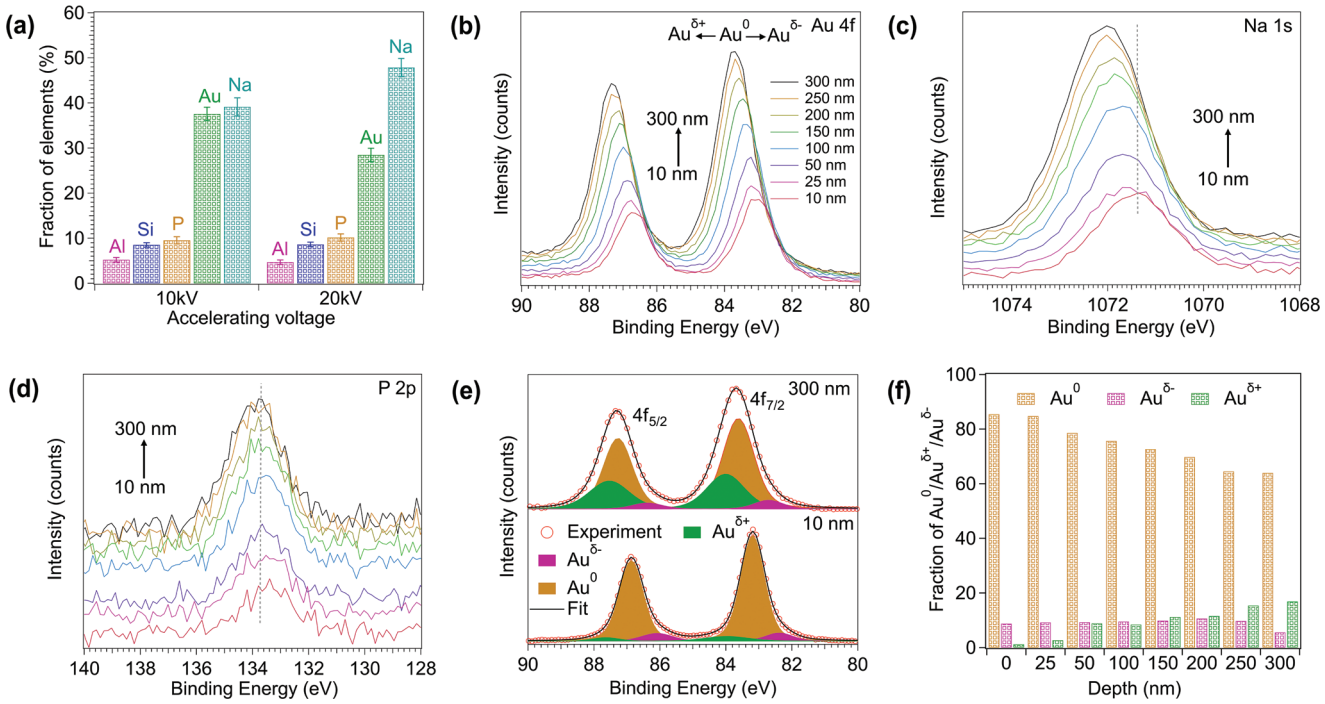

Figure 3. a) Fraction of elements in HGNI, identified using the point-based WDS technique, which also shows the fractional variations of elements at different accelerating electron voltages. b–f) XPS depth profiling investigations over a range from 10 nm to 300 nm: b–d) XPS spectra of Au 4f, Na 2s and P 2p, respectively, e) Deconvolution of Au 4f XPS spectra collected at a depth of 10 nm (bottom) and 300 nm (top), and f) Fractional variations of Au^0, $Au^{\delta+}$, and $Au^{\delta-}$ with increasing the depth from 10 to 300 nm.

electron density, this implies that the H-glass-supported HGNIs are composed of three uniquely charged Au species.

Figure 3c illustrates an increase in the binding energy of Na 1s electrons, indicating that Na acquires a more positive charge. This variation in charge implies that Na, with its electropositive nature, donates electrons, thereby enhancing the electron density at the Au ($Au^{\delta-}$), confirming the interaction between Au and Na.[42] The XRD spectrum (Figure 1e) explicitly verifies the presence of metallic Au (Au^0) in H-glass-supported HGNIs. Au 4f XPS spectrum (Figure S24, Supporting Information) for the Au film coated on H-glass shows that the $4f_{7/2}$ binding energy for metallic Au appears at 83.3 eV. Despite having lower electronegativities for Al, Si, and P at 1.61, 1.86, and 2.2, respectively, compared to Au at 2.54, these elements tend to gain electrons, which results in a reduction of electron density in Au.[42–44] Consequently, the observed peaks in the $4f_{7/2}$ binding energy approximately at 82.38, 83.18, and 83.98 eV are ascribed to negatively charged Au ($Au^{\delta-}$), metallic Au (Au^0), and positively charged Au ($Au^{\delta+}$) species, respectively. However, the peak at 83.98 eV in the Au 4f spectrum is attributed to the combined influence of interactions,[42–44] Au-P, Au-Al, and Au-Si, as per the STEM, EDS, and WDS findings. Figure 3f shows how different electronic states of Au vary in proportion at depths ranging from 10 to 300 nm. It reveals an increase in the proportion of $Au^{\delta+}$ while the fraction of $Au^{\delta-}$ remains constant. This pattern indicates a uniform diffusion of Na throughout the GNIs and a gradient diffusion of P/Al/Si. Particularly, as depicted in Figures S21 and S22 (Supporting Information), the binding energy of P 2p /Si 2p /Al 2p electrons do not exhibit significant variation with depth, despite their interactions with Au. This is likely due to the presence of enriched tetrahedral units like PO_4^{3-}, SiO_4^{4-}, and AlO_4^{5-}. XPS depth profiling reveals that Au species constitute ≈85% of the composition in HGNI/H-glass hybrids, indicating a significant presence. Further, it may be anticipated that various valence states in HGNIs improve the adsorption of water molecules and enhance electron transfer from HGNIs to the water molecules, thus facilitating the photocatalytic H_2 production.

To understand the electric field distribution in H-glass-supported HGNIs, we employed three-dimensional finite-difference time-domain (3D FDTD) simulations, **Figure 4**. A unit cell with 3D HGNIs is constructed based on SEM images (Figure S25, Supporting Information). As illustrated in Figure 4a, there is a notable increase in the localized electric field at the sharp edges of the individual Au islands upon LSPR excitation. The overall electric field intensity enhancement ($|E|^2/|E_o|^2$) of the H-Au substrates reached ≈17 times upon irradiation at 532 nm. Figure 4b provides a 3D mapping of the electric field intensity distributions around a single Au island, while Figure 4c presents the cross-sectional distribution of the electric field intensity for a single Au island enclosed within the H-glass.

In order to investigate the chemical interactions between H-Au glass and H_2O molecules, operando surface-enhanced Raman spectroscopy (SERS) measurements were carried out by applying water onto the surface of H-Au. **Figure 5a** shows the Raman spectra collected both in the presence of HGNIs (H-Au glass) and absence of HGNIs (H-glass). To consistently compare the various spectral profiles, the spectra in the 350–1900 cm^{-1} range were normalized to the peak at 1031 cm^{-1}, while spectra in the

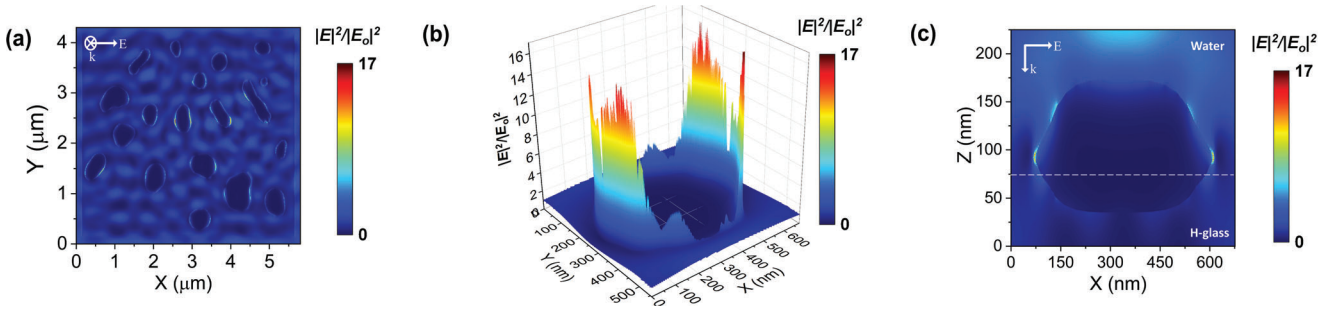

Figure 4. a) Simulated electric field intensity distribution map in the x-y plane at a wavelength of 532 nm using the FDTD method. b) Spatial distribution of scattered electric field intensity around a single particle. c) The electric field distribution of a single particle in the x-z plane. The incident light was propagated from the z-axis and polarized along the x-axis.

2400–4000 cm^{-1} range were normalized to the peak at 3400 cm^{-1}. The Raman spectrum of H_2O reveals ν(O-H) and δ(H-O-H) vibrational bands in the 3100–3800 cm^{-1} and 1550–1680 cm^{-1} regions, respectively.[45] As shown in Figure 5a, the presence of HGNIs on H-glass leads to an increase in the low-intensity δ(H-O-H) band, and the elimination peaks are ≈2972 and 3838 cm^{-1}. Additionally, there is a noticeable narrowing in the overall width of the ν(O-H) band.

Figure 5b,c illustrates the changes in the intensity of δ(H-O-H) and ν(O-H) bands and the integrated intensity ratio of ν(O-H) to δ(H-O-H) vibrations with respect to varying laser power. The inset of Figure 5b highlights a blue shift in the ν(O-H) stretching vibration with an increase in laser power. This shift is attributed to an excess of electrons, which strengthens the H_2 bonds in molecules, causing the stretching frequency to shift toward a higher wavenumber.[46] The enhancement in the δ(H-O-H) signal (Figure 5c) does not directly correlate with the laser power intensity, suggesting the presence of Fermi resonance.[45] This is due to the intramolecular inter-mode coupling between the fundamental ν(O-H) and the first overtone of the δ(H-O-H) vibrations,[46] leading to the variations in the intensities of δ(H-O-H) band.[47] Further, the observed SERS spectral variations are attributed to electron transfer to the H_2O molecule. SERS spectra, as a function of reaction time ranging from 0 to 15 min at a fixed laser power and the corresponding integrated intensity ratio of ν(O-H) to δ(H-O-H) vibrations, are shown in Figure 5d,e, respectively. The ν(O-H) vibrations do not exhibit significant variation with increasing reaction time. Nevertheless, δ(H-O-H) vibrations exhibit significant fluctuations (inset of Figure 5d). The deconvolution of δ(H-O-H) and ν(O-H) bands, as shown in Figures S26

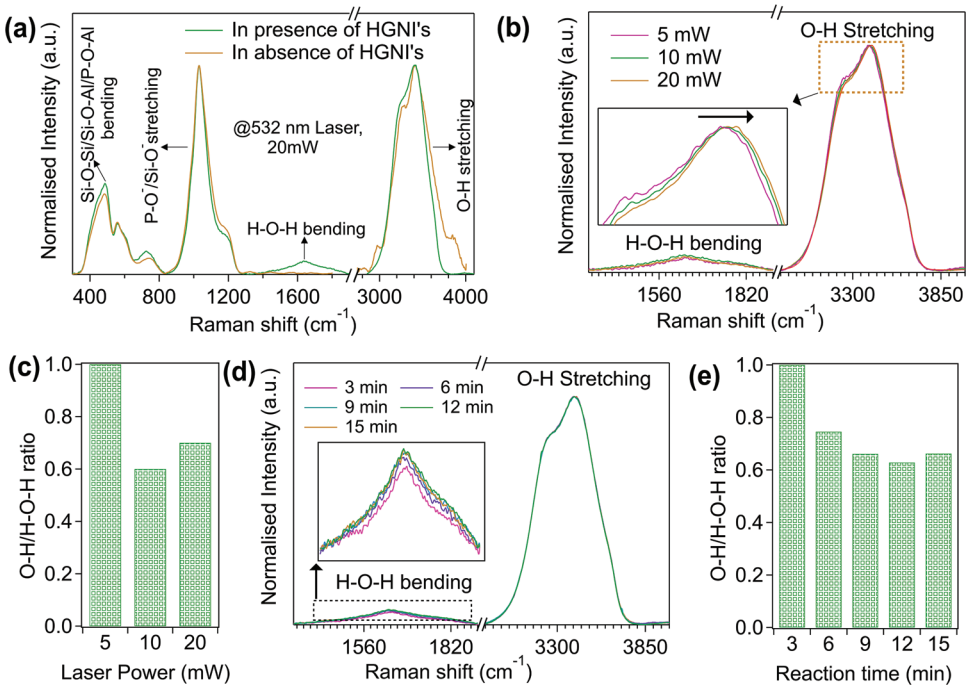

Figure 5. a) Comparison of the SERS spectra, normalized to the peak at 1031 cm^{-1}, for H_2O molecules collected in the presence of HGNIs (H-Au glass) and in the absence of HGNIs (H-glass). Variations in SERS spectra profiles for H_2O molecules with increasing laser power (b) and with increasing the reaction time (d). Variations in the integrated intensity ratio of ν(O-H) stretching vibrations to δ(H-O-H) bending vibration with varying laser power (c) and reaction time (e).

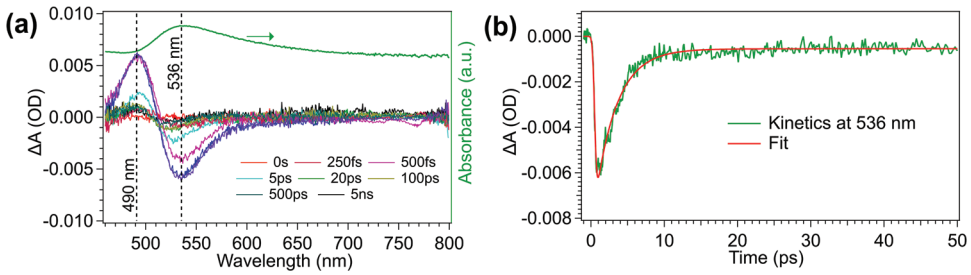

Figure 6. a) fs- transient absorption spectra recorded for H-Au glass at various time delays. b) Transient absorption kinetics for 536 nm probing wavelength.

and S27 (Supporting Information), respectively, substantiates the variations in the δ(H-O-H) vibrations. It is worth noting that δ(H-O-H) vibration is influenced by intermolecular coupling and the strength of H_2 bonding, where it appears at 1594 cm^{-1} for gas molecules and at 1643 cm^{-1} for liquid molecules.[48] In this study, an increase in the area and full width at half-maximum (FWHM) of the δ(H-O-H) vibrations at lower wavenumber (Figure S26, Supporting Information) and a decrease in the integrated intensity ratio (Figure 5e) indicate a decrease in the H_2 bond strength in the H_2O molecule over time.

To probe the electron dynamics of HGNIs embedded in H-glass, we performed the transient absorption spectroscopy (TAS) experiments using the pump-probe method. **Figure 6a** shows the fs- transient absorption spectra recorded for H-Au glass at various time delays using a 410 nm pump light with a power of 0.5 mW. Post-pulse excitation, the TA spectra reveal transient positive and negative spectral features. The positive TA change ≈490 nm corresponds to the d to sp (d-sp) interband transition of electrons in Au, while the negative TA change ≈536 nm corresponds to the bleaching of the LSPRs. The TA signal amplitude is directly proportional to the number of hot electrons,[49,50] and the fast decay of the TA bleaching signal indicates the cooling of the hot electrons. Figure 6b shows the time evolution of the TA spectrum at 536 nm, fitted with an instantaneous response function. The hot electron lifetime (τ) is determined to be 2.94 ps, extracted by fitting with the multi-exponential decay function. However, previous studies have shown that the hot electron lifetime spans from 1.2 to 2 ps for Au NPs deposited on SiO_2 glass[51] and for variously sized Au NPs.[52] It is evident that the hot electron lifetime for HGNIs extends beyond previously reported lifetimes for Au NPs. It may be noted that MNPs with a hot electron lifetime (τ) higher than ≈1.5 ps are preferred for photocatalysis.[53]

To assess the STH efficiency of the H-Au system, online gas chromatography (Figure S28, Supporting Information) was employed. **Figure 7a** shows the rate of H_2 evolution under exposure to simulated solar light (AAA class solar simulator 1 Sun, 1000 mW cm^{-2}) for durations up to 3 h. The absorption spectrum for H-Au glass (Figure 1d) spans from 480 to 700 nm, with a peak centered at 536 nm, attributed to particle size distribution. Note that, the absorptivity of either H-glass or a thick Au film remains below 10% for wavelengths beyond 600 nm. Since, the solar spectrum comprises 3% UV (300-400 nm) and 40% visible (400-700 nm) light, the wide spectral response of H-Au system ensures efficient light harvesting over a broad spectrum, covering the high-intensity portion of the solar spectrum (400–700 nm). The H-Au sample exhibits a remarkable photocatalytic activity, yielding an H_2 production rate of 6.1 mmol/h-cm^2 with the overall STH energy-conversion efficiency reaches to 0.6%. Table S1 (Supporting Information) shows a comparison of the H_2 evolution rate of different photocatalytic systems. To investigate the effect of sacrificial reagents, which act as hole acceptors, H_2 production reactions are carried out with ethanol and Na_2S/Na_2SO_4. Interestingly, H-Au demonstrates a comparable STH conversion efficiency in both deionized (DI) water and with a sacrificial agent, as shown in Figure 7b. This indicates that the H-Au can effectively produce H_2 via water splitting without requiring sacrificial reagents. Further, Figure 7c shows the trend of solar H_2 production over a 12 h period using H-Au in the presence of water and moisture. A linear increase in H_2 production is observed in both scenarios during prolonged irradiation, with a maximum of 40 mmol of H_2 generated in the presence of water after 12 h, demonstrating a production rate of approximately two orders of magnitude greater than that achieved in the presence of moisture. Additionally, the variation in STH conversion efficiency at different sun intensities over time is depicted in Figure 7d. Figure 7e shows the cyclic STH performance of the H-Au system, showing no decrease in photocatalytic activity after six cycles. The STH values are strongly influenced by both the reaction time and sun intensity, with the highest STH value of 0.6% for H-Au achieved under one sun intensity over a 3 h period. Additionally, Figures S29–S32 (Supporting Information) demonstrate the exceptional stability of H-Au, highlighting the consistent bonding and chemical composition of HGNIs after photocatalytic measurements. The slight decrease in H_2 evolution may be linked to the formation of a hydrated layer, as illustrated in Figure S32 (Supporting Information). In our previous study, we demonstrated that increasing film thickness results in larger gold nano-islands. The consequential effect of Au film thickness on STH performance was evaluated as illustrated in Figure S33 (Supporting Information). A 50 nm thick film provides HGNIs with enhanced STH performance.

Scheme 1 shows the schematic presentation of the H_2O splitting mechanism. Upon photoexcitation, resonant collective oscillations of the free electrons in the HGNIs excite LSPRs. LSPRs can localize the light at the corners/edges of the HGNIs, which are called hot-spots and the electric field intensity at the hot-spots[54,55] is extremely high. The non-radiative decay of plasmons in these hot spots results in the generation of hot electrons, which are electrons excited from the conduction band to energy states higher than the Fermi level of the metal through intraband transitions.[56,57] Hot electrons[58,59] quickly reach a Fermi-Dirac distribution[57] due to rapid thermalization processes. This

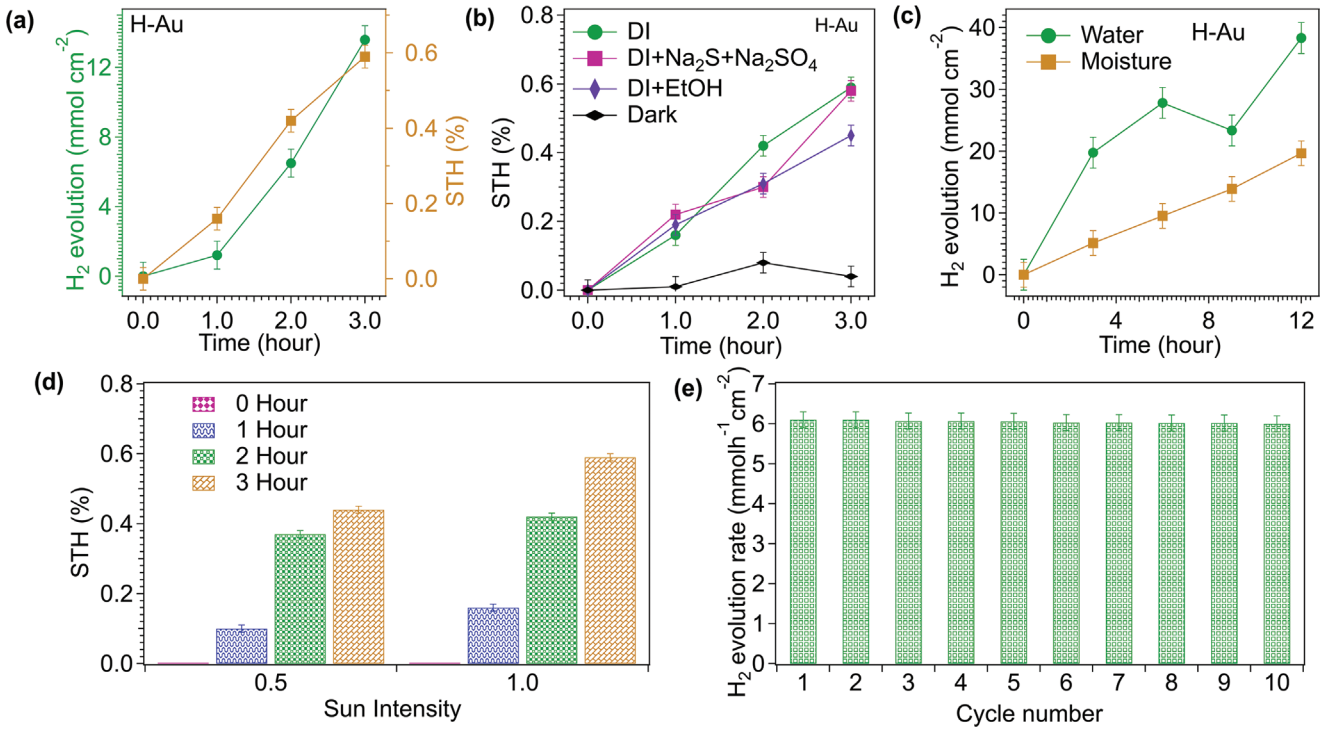

Figure 7. a) H_2 evolution rate (left axis) from liquid water, and STH conversion efficiency (right axis) using the H-Au sample as photocatalyst. b) STH conversion efficiency of H-Au in the presence of various sacrificial agents. c) Performance of H-Au sample as photocatalyst for H_2 evolution from liquid water and water moisture during the prolonged period, up to 12 h. d) STH conversion efficiency with increasing the sun intensity. e) Cycling photocatalytic performance of H-Au sample.

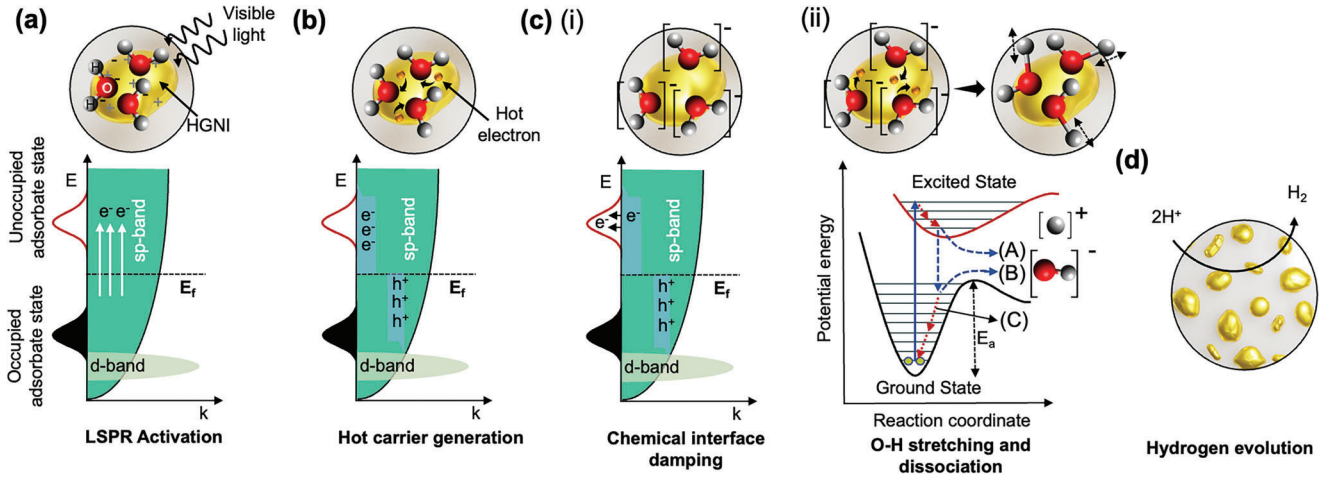

Scheme 1. Schematic picture demonstrating the photocatalytic mechanism from H-HGNIs. a) Upon light excitation, the free conduction electrons in HGNIs interacts with the electromagnetic field and oscillates collectively. The bottom figure represents the E-k diagram. On the left side of the E-k diagram, curves represent hybridized adsorbate state. The lower part of these curves indicates occupied states, while the upper part signifies unoccupied states. b) Hot electrons are generated due to the non-radiative decay of the plasmon at the hot-spots. c) (i) Due to the absence of potential barrier between the HGNI and glass, the generated hot electrons are transferred to the unoccupied adsorbate states of H_2O molecules through the CID phenomenon, and convert them into the TNI, i.e., $[H_2O]^-$. (ii) the TNIs move along the excited potential surface and gain kinetic energy, responsible for the O-H stretching vibrations. Depending on the energy level, one or more of the following events may occur: (A) H_2O adsorbates dissociate into $[H]^+$ and $[OH]^-$; (B) the adsorbates decay back to their ground state with excited vibrational energy, which lowers the energy barrier for dissociation; (C) the adsorbates release energy to their surroundings and return to the ground state. d) The produced H^+ ions eventually converted into H_2.

involves electron-electron scattering, which occurs within 100 fs to 1 ps, followed by electron-phonon scattering that takes place over 1 to 10 ps.[57,60] Eventually, this energy dissipates as heat into the surrounding environment, a process taking between 100 ps to 10 ns. In HGNIs, hot electrons possesses a lifetime of 2.94 ps, as revealed from TA spectroscopy, and they will be transferred to adsorbed H_2O molecules through the plasmon-induced chemical interface damping (CID) process.[28,61,62] The CID-mediated transfer of hot electrons predominantly occurs when chemically adsorbed molecules are involved. For the H-Au system, contact angle measurements indicate that H_2O molecules chemically adsorb more effectively to HGNIs, suggesting that the adhesive forces between water molecules and HGNIs surpass the cohesive forces, which is corroborated by the decreased contact angle on H-Au relative to pristine H-glass (Figure S34, Supporting Information). Further, SERS analyses (Figure 5) also support chemical interaction between H_2O molecules and H-glass supported HGNIs.[63] Moreover, the presence of both Au^+ and Au^- in the HGNIs likely facilitates the binding of H_2O molecules to the H-glass supported HGNIs.[63]

Consequently, the hot electrons generated in the HGNIs populate the unoccupied excited state or antibonding orbital of the adsorbed H_2O molecule through the CID,[64,65] undergo charge polarization, and form transient negative ions (TNIs), denoted as $(H_2O)^-$. These TNIs subsequently release the acquired electrons back to the HGNIs and eventually transfer vibrational energy to the H_2O molecules. This is called desorption induced by electronic transition (DIET), and it is highly used in noble metal photocatalysts.[66] Once sufficient vibrational energy is accumulated, H_2O molecules dissociate into O-H^- and H^+ ions,[28,67] as shown in Scheme 1. In time-dependent density functional theory studies, Yan et al. suggest that the direct transfer of hot electrons from the Au MNPs to strongly adsorbed water molecules[68] elongates the O-H bond, leading to the dissociation of H_2O into hydroxyl group (OH^-) and H_2 (H^+). Importantly, it should be noted that these photo-induced dissociations do not necessitate a net energy transfer to the products.[28] The H^+ ions further acquire electrons from the H-glass supported HGNIs, ultimately forming H_2.

The photocatalytic efficiency of H-HGNIs is significantly influenced by three key factors: (i) Potential barrier: The lifetime of hot electrons for metal photocatalysts lies less than 1 ps,[57] and it is too short for processes like CID. However, longer lifetimes can be achieved by preventing the carriers from flowing back to the substrate. In the HGNI substrate, a high potential barrier at the interface between metal and underlying insulator glass substrate blocks the hot electron flow, extending the lifetime for escalating CID of H_2O molecules.[31] In general, the presence of transition metals or metal oxides in oxide glasses induces electronic conductivity and thereby enhances the total conductivity of the glass system.[69] The electrical conductivity measured at various temperatures is equivalent for both H-glass and H-Au glass, as demonstrated by impedance spectroscopy results, Figure S35 (Supporting Information).[70] This clearly indicates the lack of electron transition between HGNIs and H-glass; (ii) Electric field: as revealed from FDTD simulations, strong electric fields are localized at the surfaces of the HGNIs due to the LSPR excitation. These fields alter the charge excitation process and facilitate the efficiency of charge transfer;[28,71,72] (iii) Multiple interfaces within the HGNIs: The existence of multiple interfaces between Au and Au-compounds within the HGNIs allows an energy dissipation from plasmonic Au to Au-compounds. The significant reduction in contact angle and the enhanced chemical interaction due to multiple oxidation states, coupled with the extended lifetime of hot electrons facilitated by multiple interfaces and the substantial potential barrier between the glass and HGNIs, collectively play a crucial role in improving the photocatalytic efficiency of HGNIs for visible light-driven water splitting. It should be noted that the concentration of elements from the H-glass within each HGNI at increasing depths and the specific role of Au compounds in photocatalytic performance are still subjects of active research. Furthermore, the role of the interfaces within HGNIs in relation to photocatalytic efficiency require further investigations.[35]

3. Conclusions

In summary, this work presents the integration of HGNIs on an in-house developed H-glass structure for photocatalytic applications. The H-glass-supported HGNIs act as an efficient plasmonic photocatalyst for producing H_2 through water splitting, achieving a high STH conversion rate of ≈12.5 mmol/h-cm^2 under visible light exposure and at room temperature. This high STH conversion rate is attributed to the formation of various Au oxidation states arising from the strong interaction between H-glass components (P/Al/Si/Na) and GNIs, as well as the presence of multiple interfaces within the HGNIs, which collectively facilitate charge-driven- photocatalytic reactions. This innovative approach promises efficient immobilization of similar metal catalysts, offering benefits in terms of heterogeneous durability, processability, and practical applications. Given these findings, the rational design of HGNI on H-glass appears to be an excellent method for improving charge separation and utilization, leading to highly efficient solar-to-fuel conversion systems.

4. Experimental Section

Synthesis of Glass and Deposition of HGNIs: A commercially viable melt–quenching technique was utilized to prepare the H-glass. The precise quantities of technical-grade powders of sodium carbonate (Na_2CO_3), silicon dioxide (SiO_2), ammonium dihydrogen phosphate [$(NH_4)H_2PO_4$], and aluminum oxide (Al_2O_3) were ground with isopropanol using an agate mortar and pestle for uniform mixing. Subsequently, the mixture was melted at 1600 °C for an hour in a Pt crucible. The resulting melt was then rapidly cooled in air on a preheated stainless-steel plate at 450 °C, and subsequently annealed at 600 °C for 60 min. The amorphous nature of H-glass was confirmed using the XRD profile, Figure S1 (Supporting Information). For characterization purposes, polished and cleaned glass slides of 10 × 10 × 1.5 mm^3 were utilized throughout the study. After cleaning, the glass slides were loaded in an Agar Auto Sputter Coater (Model: 108A, UK) to coat the Au thin film, with a thickness of 50±3 nm. The thickness of the deposited film was monitored using an Agar thickness monitor (Model: MTM–10). After depositing Au, the glass samples were processed for thermal heat treatment at 550±5 °C for 15 min in an ambient air atmosphere. After subjecting the glass slides to a heat treatment process, the durability and integrity of the Au layer were assessed. The glass surfaces were rubbed with a cotton cloth towel several times to remove the Au layer. The glass slides were also processed for cleaning using a similar protocol followed before initiating the Au coating on the glass substrates. The glass slides were then processed for further characterization.

Glass Transition Temperature (T_g): Specific heat (C_p) as a function of temperature from room temperature to 700 °C under N_2 atmosphere was measured for H-glass and H-AU, using the Differential Scanning Calorimetric (DSC) technique at a heating rate of 10, Kmin-^{1} using Netzsch DSC thermal analyzer (Model: 404 F3 Pegasus, Germany).

FESEM, STEM, and EDS Measurements: SEM images of embedded HGNIs on the H-glass substrate were captured using a Thermo Fisher Scientific Apreo S FESEM instrument with an accelerating voltage of 10–30 kV in the high vacuum mode. The presence of Au, P, and other elements (Na, O, Al, and Si) and their atomic percentage, elemental mapping, and line scans were acquired using an inbuilt FESEM energy-dispersive x-ray (EDAX) detector (Ultra Dry Silicon Drift Detector). EDAX detector's specified resolution was 129 eV. Pathfinder X-ray microanalysis software was used to acquire the EDAX data. High-angle annular dark-field, dark-field, and bright-field scanning transmission electron microscopy were acquired with ADF, STEM 3+ detectors. Secondary electron images were captured with an ETD detector. For STEM imaging, detached HGNIs containing acetone solvent of ≈15 µL drop-costed on the Lacey carbon-coated copper grid with a mesh size of 400. The grid was kept in a vacuum oven at 80 °C for 12 h before the microscopy experiment.

UV–Vis Absorption: Optical absorption spectra for H-glass and H-Au were recorded in the wavelength range of 250–900 nm using a Thermo Scientific UV–vis absorption spectrometer (Model: Evolution 200, U.S.). The stability of HGNIs embedded in the hosts was checked by recording the optical absorption spectra before and after cleaning with water.

XRD Measurements: XRD diffraction pattern of samples was performed in PAN analytical (X'Pert PRO, 40 kV, 30 mA, wavelength ≈0.154 nm) and Bruker AXS D8 Advanced equipment (40 kV, 40 mA, wavelength ≈0.154 nm) with Cu Kα radiation.

FDTD Simulations: Finite-difference time-domain (FDTD) simulations of HGNIs were conducted using Lumerical FDTD Solutions. The reconstructed HGNI structures were imported into the FDTD toolbox, and appropriate material properties, in terms of complex refractive indices, were assigned for both Au (following the Johnson and Christy model[73]) and H-glass chemistries. For FDTD simulations, linearly polarized light with a specific wavelength of 532 nm was introduced using a total-field/scattered-field source oriented in the -z direction. A uniform grid size was employed throughout the entire simulation volume. To analyze the electric field distribution around the HGNIs, a combination of perfectly matched layer (PML) absorbing boundary conditions and frequency domain field profile monitors was employed. Throughout these simulations, we employed water as the surrounding dielectric medium.

Ultrasonication: To remove the embedded HGNIs from the H-Au glass, ultrasonication was performed using a bath sonicator (Barson 1800, frequency of 40 kHz, Power 90 W). Initially, the substrate was kept at the bottom of a 10 mL glass vial, and then 3 mL of acetone was added. The H-Au glass with vial was bath sonicated for 3 h 30 min with different time intervals with the help of chilled water circulation. After this process, the substrate was removed from acetone. High-speed centrifugation was performed at 8000 rpm for 30 min to sediment the separated HGNIs from the glass matrix in the solvent. After centrifugation, the top 99% of the acetone was removed entirely. It was observed that a light-red-colored sample dispersed in a slightly concentrated form, ≈100 µL of HGNIs in acetone was preserved and used for further imaging analyses.

Wavelength Dispersive Spectroscopy Measurements: The electron probe microanalyzer EPMA-1720HT, manufactured by SHIMADZU in Japan, equipped with Wavelength Dispersive Spectroscopy (WDS), was utilized for chemical analysis measurements. The instrument had an energy resolution of 20 eV for WDS measurement. Within the EPMA-1720 HT, there were two spectrometer units, each set at a take-off angle of 52.5 degrees. The first unit contained RAP and PbST crystals with an EXA Detector, while the second unit featured LIF and PET crystals with an FPC Detector. During WDS measurements, all samples were exposed for 1 min at a working distance of 5 mm.

TEM Sample Preparation: Rectangular shape slices having dimensions of 2.5 × 10 × 1 mm^3 were obtained from H-Au. These slices were sandwiched using wax, so the HGNIs were located at the center. Then, the rectangular-shaped samples were converted into solid cylindrical-shaped models with diameters of 2.5 mm and lengths of 10 mm. In this solid cylinder, the HGNIs on H-Au glass lie along the cylinder's axis. Finally, the cylindrical piece was inserted into a stainless-steel cylindrical tube. A thick TEM grid sample of 250 µm with ≈2.5 mm diameter was obtained from a stainless-steel tube. The thickness of the grid-like disc was then reduced to 60 µm by polishing on both sides. Then, the 60 µm grid-like disc was dimple-grinded to 40 µm. Finally, after observing the continuity of the interface in the sample using a microscope, the grid-like disc was subjected to ion milling till the formation of lens shape at the interface.

TEM Measurements: The morphology and high-resolution lattice images of the HGNIs were obtained using a transmission electron microscope (JEOL 2100 Plus) fitted with a single crystal of lanthanum hexaboride (LaB_6) thermionic emission gun. HR-TEM images were obtained at an accelerated voltage of 200 kV in the high-vacuum mode. Oxford X-Max EDAX detector was used for elemental analysis. EDAX detector was made on a large-area Silicon Drift Detector (SDD) with an active area of 80 mm^2. The specified energy resolution was 129 eV, and the detector contained an SATW ultra-thin polymer window. The electron beam resolution was 0.19 nm. The suspended HGNIs in acetone were re-dispersed using bath sonication before depositing on a Lacey holey carbon TEM grid and subjected to 12 h at 60 °C in a vacuum oven and used thereafter for electron microscopy analysis.

XPS Depth Profile Measurements: The XPS experiment, which aimed to determine the surface oxidation states of individual chemical entities, was conducted using a PHI 5000 Versa Probe II instrument manufactured by Physical Electronics, U.S. Monochromatic aluminum K-alpha X-ray with a photon energy of 1486.7 eV and diameter 400 micrometer was employed as its source. The measurements were conducted with a pass energy of 11.75 eV and a step size of 0.10 eV. XPS depth profiling refers to a technique wherein the composition and chemical information of materials are analyzed at various depths below the surface. XPS depth profile spectra were acquired to investigate how the elemental and chemical composition of H-Au glass changes as a function of depth, providing insights into surface and near-surface characteristics. For depth profiling, an Ar^+ ion gun with an energy of 2000 eV was employed for sputtering, with a sputtering rate of 0.49 nm/s. The XPS depth profiling process achieved a total depth of 300 nm through etching by multiple sputtering cycles.

XPS spectra were analyzed with the help of the CASA program. The quantitative analysis of various oxidation states of constituents was done by calculating the area under the corresponding deconvoluted curves. The deconvolution of the peaks was carried out based on the three parameters, first: keeping the area ratio of $4f_{7/2}$ and $4f_{5/2}$ as 4:3, second: maintaining the spin-orbit separation distance of 3.67 eV between $4f_{7/2}$ and $4f_{5/2}$, third: retaining the FWHM of $4f_{7/2}$ and $4f_{5/2}$ same.

Atomic Force Microscopy: Atomic force microscopy (AFM) characterization was performed to measure the diameter and depth of the cavity created after subjecting the H-Au glass to ultrasonication in non-contact mode using a Park Systems XE7 model. A cantilever with a Si tip of ≈10 µm in length for the AFM analysis was utilized. AFM images were acquired with a resolution of 256 × 256 image pixels, a resonance frequency of 325 kHz, an amplitude of 36.74 nm, and a set point of 15 nm. Initially, a 3D topography image of a 10 µm × 10 µm area was obtained to distinguish between the embedded and removed HGNI particles on the substrate. Once the embedded and removed particles became clearly visible, a smaller topography scan of ≈4 µm × 4 µm in size was conducted. This allowed to observe the depth (Cd-Largest distance from the surface) and diameter (CD-largest distance across X) of the cavities of the removed particles, as shown in Figures S5 and S7 (Supporting Information). The values of height profiles, $C_{D,}$ and C_d are measured for 20 cavities using AFM imaging processing software (XEI).

Photocatalytic Measurements: The photochemical conversion experiments were performed in a customized 30 mL volume. The outer body was made of Al, and light passed through a 10 mm thick fused quartz plate, which was used to pass UV-Vis-NIR regions of light when required. In all the experimental studies, A catalyst and 5 ml of type 1 water (18.2 MΩ.cm LABJAL) were placed in a circular glass petri dish (3.8 cm inner diameter). AAA class solar simulator equipped with 300 W Xenon lamp and AM 1.5G filter (Sciencetech, Canada) is used to illuminate 1 SUN, and the

Sun level of solar simulators was monitored and verified using the SSIVT-REF (125-9007) single element silicon detector. The SSIVT-REF detector was calibrated to the NIST traceable calibrated reference cell and was effective for sensing wavelengths between 190 nm and 1100 nm. The reactor was filled with inert gas 99.999% Argon of 2 bar against atmosphere pressure, and the reactor outlet was connected to the gas chromatography (TRACE 1310, Thermo scientific equipped with a thermal conductivity detector (TCD)) injection port online. A sample of 1 mL gas was injected for quantification of H_2 evolution after every hour of light illumination. Before light illumination, a degassing process was performed by flushing Argon gas to remove any residual gases from the whole system; this process was repeated thrice.

Solar/Visible Light-to-Hydrogen (STH) Energy Conversion: The standard protocol for the STH conversion efficiency was followed as follows:

$$STH\ (\%) = 100 \times \frac{Output\ energy\ as\ H_2}{Energy\ of\ Incident\ solar\ light}$$

$$= 100 \times \frac{rH_2\left(\frac{mol}{Sec}\right)\Delta G_r\left(\frac{J}{mol}\right)}{P_{Sun}\left(\frac{W}{m2}\right)\ S\left(m^2\right)} \quad (1)$$

where P_{sun} is the energy flux of sunlight (1 Sun = 1000 W m^{-2}), S is the irradiated area (=0.0001 m^2), rH_2 is the rate of H_2 production (see the supporting Excel Sheet Data S1), and ΔG_r is the reaction Gibbs energy (=235000 J mol^{-1}).

SERS Measurements: Surface-Enhanced Raman Spectroscopy (SERS) measurements were conducted utilizing a confocal LabRAM HR800 Raman spectrometer (HORIBA Jobin Yvon). The excitation source employed for these experiments was a 532 nm wavelength laser (Nd–YAG, Oxxius) operating at various power levels, specifically 5 mW, 10 mW, and 20 mW. To capture the Raman signals, 600 grooves/mm grating was utilized along with a 50 × long working distance objective lens featuring an 8 mm working distance. A Synapse charge-coupled-device (CCD) camera was employed for data collection. The resulting spot size achieved in the measurements was ≈2 µm. To investigate the time-dependent behavior of the samples under examination, Raman spectra were acquired over a period ranging from 3 to 15 mins during continuous illumination with the 532 nm laser at different power levels.

Transient Absorption Spectroscopy: Transient absorption spectroscopy (TAS) was carried out on the H-Au sample using the optical pulse source from a Ti: sapphire crystal laser amplifier (Micra, Coherent) (35 fs, 4 mJ/pulse, 1 kHz, 800 nm). A beam splitter was used to split the beam into two parts (70:30 ratio). A TOPAS-C, an optical parametric amplifier, was used to vary the wavelength of the high-intensity beam (pump) from 190 to 2600 nm. A sapphire crystal was used to convert the low-intensity beam (probe) into a white light continuum. Both the pump and probe were spatially overlapped on the sample. The transient absorption spectra (optical density) were expressed in terms of the difference in absorbance of the sample with and without the pump.

Contact Angle Measurements: The contact angles of H– and H–Au glasses were measured at room temperature utilizing an automatically controlled droplet volume, followed by axisymmetric drop shape analysis via Image J software. The Ossila contact angle Goniometer (model: L2004A1, UK), which uses a CCD camera for the measurement of surface tension and image analysis processing software, was utilized for the contact angle measurements. The deionized water droplet volume was 0.5 µL and was recorded 3 s after the drop was deposited on the glass substrates.

Supporting Information

Supporting Information is available from the Wiley Online Library or from the author.

Acknowledgements

I.M., J.G., S.G., and A.R.A. acknowledge the technical support from Nabanita Chakrabarti, Sanjib Samaddar, Debayan Gupta, Debabrata Biswas, Satyendra Nath Barik, and Tapas Misra. The authors are thankful to the Director, CSIR-CGCRI, and to the Director of CSIR-NPL for their kind support. The authors thank Dr. Swastik Mondal and Dr. Jayanthi K. for the helpful discussion. A.R.A. thanks Dr. A. R. Molla for supporting the synthesis of glasses. Funding: This work was supported by the Science and Engineering Research Board (SERB), DST, Govt. of India, through the Early Career Research Award (ECR/2018/000292). Part of the work was supported by the Council of Scientific and Industrial Research (CSIR), Govt. of India, under "CSIR Hydrogen Technology (H2T)-Mission Program". P.T. would like to thank SERB (CRG/2022/002871) for financial support. P.J.G. acknowledges CSIR, New Delhi, for providing CSIR–RA fellowship (31/015(0158)/2020–EMR–I). S.G. thanks SERB for the POWER Grant (SPG/2020/000720) and "DST–IIT Delhi Energy Storage Platform on Batteries" (DST/TMD/MECSP/2K17/07) for infrastructure. E.V, A.S, and V.R. acknowledges SRM IST Kattankulathur for a start-up grant, infrastructure, and DST for partial financial support (INT/RUS/RFBR/386). EV acknowledges Mr. Vadivel B, Senior Scientific Officer at SRM IST (KTR Campus) for technical assistance in HAADF-TEM imaging. Thanks to Dr. D. Althaf Basha for the discussions on electron microscopy data. M.M. thanks for the support of the DST-INSPIRE faculty scheme (DST/INSPIRE/04/2017/001392). K.D.M.R. acknowledges TRC and Science and Engineering Research Board (SERB) project CRG/2022/004873 for financial support. P.R. thanks DST for sanctioning the INSPIRE fellowship (DST/INSPIRE Fellowship/2018/IF180761). M.C. acknowledges the financial support from the Novo Nordisk Foundation under the grant Nanoscale Energy Generators (number NNF20OC0064735).

Conflict of Interest

The authors declare no conflict of interest.

Data Availability Statement

The data that support the findings of this study are available on request from the corresponding author. The data are not publicly available due to privacy or ethical restrictions.

Keywords

glass, gold nanoisland, multiple interfaces, oxidation state, photocatalysis

Received: February 13, 2024
Revised: March 16, 2024
Published online: April 2, 2024

[1] X. M. C. Ta, R. Daiyan, T. K. A. Nguyen, R. Amal, T. Tran-Phu, A. Tricoli, *Adv. Energy Mater.* **2022**, *12*, 2201358.
[2] P. J. Megía, A. J. Vizcaíno, J. A. Calles, A. Carrero, *Energy Fuels* **2021**, *35*, 16403.
[3] Z. Abdin, A. Zafaranloo, A. Rafiee, W. Mérida, W. Lipiński, K. R. Khalilpour, *Renewable Sustainable Energy Rev.* **2020**, *120*, 109620.
[4] L. Huang, B. Li, B. Su, Z. Xiong, C. Zhang, Y. Hou, Z. Ding, S. Wang, *J. Mater. Chem. A* **2020**, *8*, 7177.
[5] B. Su, M. Zheng, W. Lin, X. F. Lu, D. Luan, S. Wang, X. W. (David) Lou, *Adv. Energy Mater.* **2023**, *13*, 2203290.
[6] Z. Xiong, Y. Hou, R. Yuan, Z. Ding, W. J. Ong, S. Wang, *Acta Phys. -Chim. Sin.* **2022**, *38*, 2111021.

[7] D. Tonelli, L. Rosa, P. Gabrielli, K. Caldeira, A. Parente, F. Contino, *Nat. Commun.* **2023**, *14*, 5532.
[8] J. M. Bracci, E. D. Sherwin, N. L. Boness, A. R. Brandt, *Nat. Commun.* **2023**, *14*, 7391.
[9] S. Shiva Kumar, V. Himabindu, *Mater. Sci. Energy Technol.* **2019**, *2*, 442.
[10] J. Jia, L. C. Seitz, J. D. Benck, Y. Huo, Y. Chen, J. W. D. Ng, T. Bilir, J. S. Harris, T. F. Jaramillo, *Nat. Commun.* **2016**, *7*, 13237.
[11] S. Ghosh, N. A. Kouamé, L. Ramos, S. Remita, A. Dazzi, A. Deniset-Besseau, P. Beaunier, F. Goubard, P.-H. Aubert, H. Remita, *Nat. Mater.* **2015**, *14*, 505.
[12] W. Li, Y. Dang, J. Li, T. Ma, G. Liao, F. Gao, W. Duan, J. Li, X. Wang, C. Wang, *Chem. Eng. J.* **2023**, *472*, 144793.
[13] T. Ma, W. Li, J. Li, W. Duan, F. Gao, G. Liao, J. Li, C. Wang, *J. Colloid Interface Sci.* **2024**, *658*, 476.
[14] M. Torras, P. Molet, L. Soler, J. Llorca, A. Roig, A. Mihi, *Adv. Energy Mater.* **2022**, *12*, 2103733.
[15] E. Bonmatí, A. Casanovas, I. Angurell, J. Llorca, *Top. Catal.* **2015**, *58*, 77.
[16] A. V. Puga, A. Forneli, H. García, A. Corma, *Adv. Funct. Mater.* **2014**, *24*, 241.
[17] M. Herran, A. Sousa-Castillo, C. Fan, S. Lee, W. Xie, M. Döblinger, B. Auguié, E. Cortés, *Adv. Funct. Mater.* **2022**, *32*, 2203418.
[18] Q. Wang, K. Domen, *Chem. Rev.* **2020**, *120*, 919.
[19] S. Ghosh, S. Bera, S. Sardar, S. Pal, F. V. A. Camargo, C. D'Andrea, G. Cerullo, *ACS Appl. Mater. Interfaces* **2023**, *15*, 18867.
[20] S. Ghosh, H. Remita, R. N. Basu, *Appl. Catal., B* **2018**, *239*, 362.
[21] S. Chen, T. Takata, K. Domen, *Nat. Rev. Mater.* **2017**, *2*, 17050.
[22] C. S. Gopinath, N. Nalajala, *J. Mater. Chem. A* **2021**, *9*, 1353.
[23] H. Nishiyama, T. Yamada, M. Nakabayashi, Y. Maehara, M. Yamaguchi, Y. Kuromiya, Y. Nagatsuma, H. Tokudome, S. Akiyama, T. Watanabe, R. Narushima, S. Okunaka, N. Shibata, T. Takata, T. Hisatomi, K. Domen, *Nature* **2021**, *598*, 304.
[24] A. Xiong, G. Ma, K. Maeda, T. Takata, T. Hisatomi, T. Setoyama, J. Kubota, K. Domen, *Catal. Sci. Technol.* **2014**, *4*, 325.
[25] Y. Goto, T. Hisatomi, Q. Wang, T. Higashi, K. Ishikiriyama, T. Maeda, Y. Sakata, S. Okunaka, H. Tokudome, M. Katayama, S. Akiyama, H. Nishiyama, Y. Inoue, T. Takewaki, T. Setoyama, T. Minegishi, T. Takata, T. Yamada, K. Domen, *Joule* **2018**, *2*, 509.
[26] V. G. Rao, U. Aslam, S. Linic, *J. Am. Chem. Soc.* **2019**, *141*, 643.
[27] A. Naldoni, V. M. Shalaev, M. L. Brongersma, *Science* **2017**, *356*, 908.
[28] U. Aslam, V. G. Rao, S. Chavez, S. Linic, *Nat. Catal.* **2018**, *1*, 656.
[29] M. Sankar, Q. He, R. V. Engel, M. A. Sainna, A. J. Logsdail, A. Roldan, D. J. Willock, N. Agarwal, C. J. Kiely, G. J. Hutchings, *Chem. Rev.* **2020**, *120*, 3890.
[30] M. Monai, K. Jenkinson, A. E. M. Melcherts, J. N. Louwen, E. A. Irmak, S. Van Aert, T. Altantzis, C. Vogt, W. van der Stam, T. Duchoň, B. Šmíd, E. Groeneveld, P. Berben, S. Bals, B. M. Weckhuysen, *Science* **2023**, *380*, 644.
[31] S. Mukherjee, L. Zhou, A. M. Goodman, N. Large, C. Ayala-Orozco, Y. Zhang, P. Nordlander, N. J. Halas, *J. Am. Chem. Soc.* **2014**, *136*, 64.
[32] A. A. Herzing, C. J. Kiely, A. F. Carley, P. Landon, G. J. Hutchings, *Science* **2008**, *321*, 1331.
[33] Z. Zhang, Y. Chen, L. Zhou, C. Chen, Z. Han, B. Zhang, Q. Wu, L. Yang, L. Du, Y. Bu, P. Wang, X. Wang, H. Yang, Z. Hu, *Nat. Commun.* **2019**, *10*, 1657.
[34] P.-C. Chen, X. Liu, J. L. Hedrick, Z. Xie, S. Wang, Q.-Y. Lin, M. C. Hersam, V. P. Dravid, C. A. Mirkin, *Science* **2016**, *352*, 1565.
[35] P.-C. Chen, M. Liu, J. S. Du, B. Meckes, S. Wang, H. Lin, V. P. Dravid, C. Wolverton, C. A. Mirkin, *Science* **2019**, *363*, 959.
[36] Z. Xu, X. Zhang, X. Wang, J. Fang, Y. Zhang, X. Liu, W. Zhu, Y. Yan, Z. Zhuang, *ACS Nano* **2021**, *15*, 7131.
[37] H. Kim, T. Y. Yoo, M. S. Bootharaju, J. H. Kim, D. Y. Chung, T. Hyeon, *Adv. Sci.* **2022**, *9*, 2104054.
[38] Y. Yao, Q. Dong, A. Brozena, J. Luo, J. Miao, M. Chi, C. Wang, I. G. Kevrekidis, Z. J. Ren, J. Greeley, G. Wang, A. Anapolsky, L. Hu, *Science* **2022**, *376*, eabn3103.
[39] J. Gangareddy, P. Rudra, M. Chirumamilla, S. Ganisetti, S. Kasimuthumaniyan, S. Sahoo, K. Jayanthi, J. Rathod, V. R. Soma, S. Das, N. N. Gosvami, N. M. A. Krishnan, K. Pedersen, S. Mondal, S. Ghosh, A. R. Allu, *Small* **2024**, *20*, 2303688.
[40] B. Jiang, Y. Yuan, W. Wang, K. He, C. Zou, W. Chen, Y. Yang, S. Wang, V. Yurkiv, J. Lu, *Nat. Commun.* **2021**, *12*, 5661.
[41] A. M. Venezia, *Catal. Today* **2003**, *77*, 359.
[42] F. Stegemann, C. Benndorf, Y. Zhang, M. Bartsch, H. Zacharias, B. P. T. Fokwa, H. Eckert, O. Janka, *Inorg. Chem.* **2017**, *56*, 1919.
[43] C. Lenardi, J. Mayer, G. Faraone, J. Cardoso, S. Marom, R. Modi, A. Podestà, S. Kadkhodazadeh, M. Di Vece, *Langmuir* **2020**, *36*, 939.
[44] W. Jeitschko, M. H. Moller, *Acta Cryst.* **1979**, *35*, 573.
[45] S. Ashihara, N. Huse, A. Espagne, E. T. J. Nibbering, T. Elsaesser, *J. Phys. Chem. A* **2007**, *111*, 743.
[46] T. Seki, K.-Y. Chiang, C.-C. Yu, X. Yu, M. Okuno, J. Hunger, Y. Nagata, M. Bonn, *J. Phys. Chem. Lett.* **2020**, *11*, 8459.
[47] A. A. Kananenka, J. L. Skinner, *J. Chem. Phys.* **2018**, *148*, 244107.
[48] G.-H. Deng, Y. Shen, H. Chen, Y. Chen, B. Jiang, G. Wu, X. Yang, K. Yuan, J. Zheng, *J. Phys. Chem. Lett.* **2019**, *10*, 7922.
[49] L. Pan, J. H. Kim, M. T. Mayer, M.-K. Son, A. Ummadisingu, J. S. Lee, A. Hagfeldt, J. Luo, M. Grätzel, *Nat. Catal.* **2018**, *1*, 412.
[50] J. Guo, Y. Zhang, L. Shi, Y. Zhu, M. F. Mideksa, K. Hou, W. Zhao, D. Wang, M. Zhao, X. Zhang, J. Lv, J. Zhang, X. Wang, Z. Tang, *J. Am. Chem. Soc.* **2017**, *139*, 17964.
[51] G. Tagliabue, J. S. DuChene, M. Abdellah, A. Habib, D. J. Gosztola, Y. Hattori, W.-H. Cheng, K. Zheng, S. E. Canton, R. Sundararaman, J. Sá, H. A. Atwater, *Nat. Mater.* **2020**, *19*, 1312.
[52] G. V. Hartland, *Chem. Rev.* **2011**, *111*, 3858.
[53] D. Peckus, A. Tamulevičienė, K. Mougin, A. Spangenberg, L. Vidal, Q. Bauerlin, M. Keller, J. Henzie, L. Puodžiukynas, T. Tamulevičius, S. Tamulevičius, *Opt. Express* **2022**, *30*, 27730.
[54] J. A. Schuller, E. S. Barnard, W. Cai, Y. C. Jun, J. S. White, M. L. Brongersma, *Nat. Mater.* **2010**, *9*, 193.
[55] A. Alabastri, A. Toma, C. Liberale, M. Chirumamilla, A. Giugni, F. De Angelis, G. Das, E. Di Fabrizio, R. P. Zaccaria, *Opt. Express* **2013**, *21*, 7538.
[56] E. Cortés, W. Xie, J. Cambiasso, A. S. Jermyn, R. Sundararaman, P. Narang, S. Schlücker, S. A. Maier, *Nat. Commun.* **2017**, *8*, 14880.
[57] M. L. Brongersma, N. J. Halas, P. Nordlander, *Nat. Nanotechnol.* **2015**, *10*, 25.
[58] S. Linic, U. Aslam, C. Boerigter, M. Morabito, *Nat. Mater.* **2015**, *14*, 567.
[59] H. Reddy, K. Wang, Z. Kudyshev, L. Zhu, S. Yan, A. Vezzoli, S. J. Higgins, V. Gavini, A. Boltasseva, P. Reddy, V. M. Shalaev, E. Meyhofer, *Science* **2020**, *369*, 423.
[60] G. V. Hartland, *Chem. Rev.* **2011**, *111*, 3858.
[61] P. Christopher, H. Xin, A. Marimuthu, S. Linic, *Nat. Mater.* **2012**, *11*, 1044.
[62] L. Zhou, D. F. Swearer, C. Zhang, H. Robatjazi, H. Zhao, L. Henderson, L. Dong, P. Christopher, E. A. Carter, P. Nordlander, N. J. Halas, *Science* **2018**, *362*, 69.
[63] J.-F. Li, Y.-F. Huang, S. Duan, R. Pang, D.-Y. Wu, B. Ren, X. Xu, Z.-Q. Tian, *Phys. Chem. Chem. Phys.* **2010**, *12*, 2493.
[64] M. J. Kale, P. Christopher, *Science* **2015**, *349*, 587.
[65] K. Wu, J. Chen, J. R. McBride, T. Lian, *Science* **2015**, *349*, 632.
[66] K. H. Kim, K. Watanabe, D. Mulugeta, H.-J. Freund, D. Menzel, *Phys. Rev. Lett.* **2011**, *107*, 47401.

[67] J. W. Gadzuk, *J. Chem. Phys.* **1983**, *79*, 6341.
[68] L. Yan, F. Wang, S. Meng, *ACS Nano* **2016**, *10*, 5452.
[69] L. Ouachouo, H. Es-soufi, M. I. Sayyed, L. Bih, *Ceram. Int.* **2023**, *49*, 28580.
[70] R. Harizanova, R. Keding, C. Rüssel, *J. Non-Cryst. Solids* **2008**, *354*, 65.
[71] E. Kazuma, J. Jung, H. Ueba, M. Trenary, Y. Kim, *Science* **2018**, *360*, 521.
[72] E. Kazuma, M. Lee, J. Jung, M. Trenary, Y. Kim, *Angew. Chem., Int. Ed.* **2020**, *59*, 7960.
[73] P. B. Johnson, R. W. Christy, *Phys. Rev. B* **1972**, *6*, 4370.